Solar RRL
www.solar-rrl.com

Antisolvent-Mediated Air Quench for High-Efficiency Air-Processed Carbon-Based Planar Perovskite Solar Cells

*Jacob Wall, Kausar Khawaja, Wenjun Xiang, Adam Dvorak, Christopher Picart, Xiaoyu Gu, Lin Li, Nicholas Rolston, Kai Zhu, Joseph J. Berry, and Feng Yan**

Perovskite solar cells (PSCs) have emerged as a leading low-cost photovoltaic technology, achieving power conversion efficiencies (PCEs) of up to 26.1%. However, their commercialization is hindered by stability issues and the need for controlled processing environments. Carbon-electrode-based PSCs (C-PSCs) offer enhanced stability and cost-effectiveness compared to traditional metal-electrode PSCs, i.e., Au and Ag. However, processing challenges persist, particularly in air conditions where moisture sensitivity poses a significant hurdle. Herein, a novel air processing technique is presented for planar C-PSCs that incorporates antisolvent vapors, such as chlorobenzene, into a controlled air-quenching process. This method effectively mitigates moisture-induced instability, resulting in champion PCEs exceeding 20% and robust stability under ambient conditions. The approach retains 80% of initial efficiency after 30 h of operation at maximum power point without encapsulation. This antisolvent-mediated air-quenching technique represents a significant advancement in the scalable production of C-PSCs, paving the way for future large-scale deployment.

1. Introduction

Perovskite solar cells (PSCs) have been demonstrated potential as an efficient and scalable photovoltaic technology,[1] with certified power conversion efficiencies (PCEs) exceeding 26%.[2] However, the commercialization of PSCs has been hindered due to perovskite instabilities associated with the material's sensitivity to fabrication conditions[3] and the fast ion migration during solar cell operating conditions.[4] A promising approach to improve the stability of PSCs is the replacement of the costly noble metal electrodes (i.e., Au or Ag) with carbon-based electrodes to prevent iodine migration and reaction with metal electrodes.[5] It has been demonstrated that hydrophobic carbon materials can repel moisture and slow down the migration of halide ions in PSCs.[6] Although the gap in efficiency between carbon-electrode-based planar PSCs (C-PSCs) and Au-electrode-based PSCs (Au-PSCs) was substantial, in recent years it has narrowed significantly. Now, C-PSCs can achieve PCEs greater than 20% by improving the conductivity of the carbon electrode, which paves the way for more stable and cost-effective PSCs.[7,8] Traditionally, C-PSCs are majorly processed in dry, inert environments, e.g., dry N_2, which limits the cost reduction and large-area manufacturability of perovskite solar modules. Recently, air-processed C-PSCs with high efficiencies above 20% have been processed in environments of RH as high as 70–80%.[8–11] Therefore, manufacturing PSCs in air conditions remains a challenge and must be addressed to ensure the scalability of the technology.

Ambient air conditions are especially difficult for fabricating PSCs because metal-halide perovskites are notoriously sensitive to the moisture level in the air.[12] Though certain reports have indicated that a small amount of water in precursor solutions may be beneficial for the surface morphology and crystallization of perovskite films, ambient processing in humid environments (RH > 30%) has proven to be difficult for PSCs.[13] Perovskite films deposited in high relative humidity environments may experience incomplete and uncontrolled nucleation, causing the resulting films to have poor surface morphology, reduced grain size, and decreased device performance.[14–17] Additives, new solvents, and interfacial engineering have been introduced to combat moisture-induced instability during the ambient processing of PSCs.[18–21] However, these approaches can be complicated and expensive to reproduce in practicality.

Precise control over the crystallization kinetics during perovskite film growth is extremely important in producing highly

J. Wall, K. Khawaja, W. Xiang, A. Dvorak, C. Picart, X. Gu, L. Li, F. Yan
School for Engineering of Matter, Transport, and Energy
Arizona State University
Tempe, AZ 85282, USA
E-mail: fengyan@asu.edu

N. Rolston
School of Electrical, Computer, and Energy Engineering
Arizona State University
Tempe, AZ 85282, USA

K. Zhu, J. J. Berry
National Renewable Energy Laboratory
Golden, CO 80401, USA

J. J. Berry
Renewable and Sustainable Energy Institute
University of Colorado Boulder
Boulder, CO 80309, USA

J. J. Berry
Department of Physics
University of Colorado Boulder
Boulder, CO 80309, USA

The ORCID identification number(s) for the author(s) of this article can be found under https://doi.org/10.1002/solr.202400599.

DOI: 10.1002/solr.202400599

efficient and stable PSCs. Particularly, this becomes imperative when attempting to process in air environments. To accelerating perovskite solvent vaporization and promote perovskite crystallization, antisolvents (ATSs) such as chlorobenzene (CB) during the perovskite film casting, vacuum, and gas quenching such as air or N_2 to promote the evaporation of solvents,[22,23] e.g., dimethylsulfoxide (DMSO) and dimethylformamide (DMF). However, the ATS approach is not easily transferable to large-area perovskite film coating techniques, such as blade or slot die coating. While gas quenching during blade coating has become more popular through an air knife, significant tuning of the gas conditions is necessary to eliminate uniformity issues for the coated perovskite films. Hence, it is imperative to leverage the advantages of both ATS and gas quenching for the enhancement of perovskite film formation.

In this study, we demonstrate an economic fabrication process tailored for use in air environments that can produce highly efficient C-PSCs by utilizing an ATS-mediated air-quench approach. By incorporating ATS vapor into the quenching air gas, C-PSCs can reap both the benefits of the ATS and the gas quench approaches, successfully converting the perovskite film completely from the intermediate phases to the photoactive phase and protecting the film from moisture attack during deposition. C-PSCs can be fabricated in ambient air with enhanced device performance and stability through this innovative approach, resulting in a champion PCE of ≈20% for C-PSCs while improving stability with respect to maximum power point tracking.

2. Results and Discussion

As shown in **Figure 1**a, we introduced a combinational quenching method by utilizing an ATS-modified quenching gas, which can provide benefits of both the ATS quenching method and the gas quenching approach during the perovskite layer deposition. Here, we use CB as a representative of the ATSs during this study. However, other ATSs have been tested in addition, such as isopropanol (IPA), diethyl ether (DEE), toluene, and ethanol. The results are shown in Figure S1, Supporting Information, and a comparison of the physiochemical properties of the solvents is shown in Table S1, Supporting Information. It is known that the various rates of solvent evaporation directly influence the formation of the perovskite nuclei and subsequently control

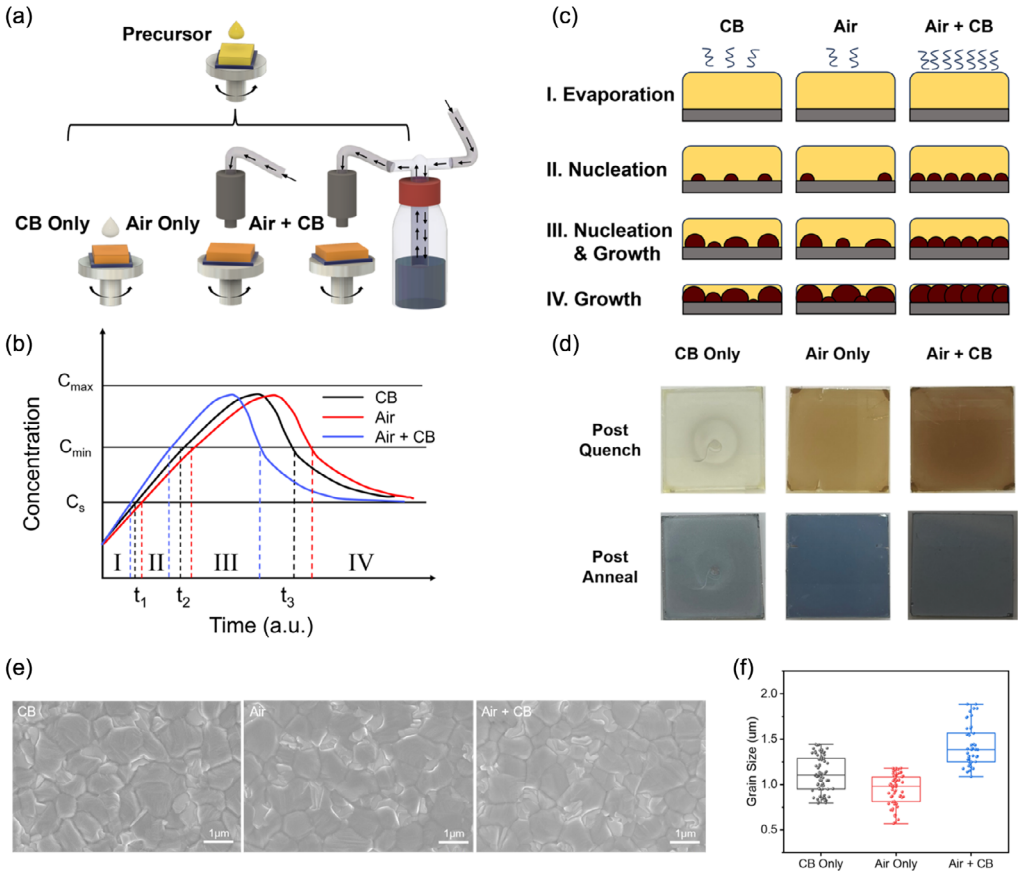

Figure 1. Antisolvent-mediated air-quench approach. a) Schematic of perovskite deposition with various quenching methods. b) The LaMer model is shown for the CB quench method (black curve), the air-quench method (red curve), and the combined air + CB quench method (blue curve). c) The behavior of perovskite nuclei with different rates of solvent evaporation. d) Images of the perovskite films as deposit and postannealing when using the three different quench methods. e) Surface morphology SEM images of perovskite films prepared with CB, air, and air + CB quenching methods, f) grain size statistics of perovskite films using the three different quench methods.

the transition of the intermediate perovskite phase, i.e., δ-phase, transition to photoactive α-phase of the film postdeposition.[24] As shown in Figure 1a, the dry air gas was transported through the CB ATS bottle carrying CB vapor for the air quench during the spin coating of the perovskite film (labeled as air + CB). Specifically, in-house dry air with RH ≈3% was chosen as the quenching gas due to its wide availability and low cost.

The crystallization mechanisms of perovskite thin films can be understood through the LaMer model as shown in Figure 1b.[25,26] Four key stages occur during the perovskite film deposition: In stage I, the precursor concentration gradually reaches a saturation point (C_s) as the solvent begins to evaporate, and the perovskite precursor ink is spread out evenly on the substrate. In stage II, a few initial nuclei form. As the solvent continues to evaporate, the solute content increases as well. Eventually, the solution becomes supersaturated, reaching the minimum concentration for nucleation to begin (C_{min}), and nucleation occurs rapidly until the solute is consumed and the concentration drops back below C_{min} (stage III). After this point, only the crystalline growth remains, and it primarily occurs through diffusion processes such as Ostwald ripening.[26] Here, the conventional ATS quickly removes most of the solvent during spin coating, while the pure air gas quench may result in slower solvent extraction than ATS. By combining the CB and air-quench approaches, we expect a medium solvent evaporation to provide a mild rate of film growth.

Figure 1c shows a schematic of the stages of perovskite nucleation and growth based on the different evaporation stages that result from the quenching methods shown in Figure 1b. The air + CB quench can increase solvent evaporation compared with the single CB or air-quench process alone. Therefore, this CB-mediated air quench promises the formation of a dense and compact perovskite film. As shown in Figure 1d, the post-spin-coated CB and air-quenched perovskite films still show transparent and light colors, respectively, due to the residual solvents (DMF and DMSO), while the as-casted air + CB-quenched films show a dark color, indicating a phase transformation from the yellow, δ-phase $FAPbI_3$ to the black, α-phase $FAPbI_3$ during the CB-mediated air-quench process.[27] The pure air quench leads to the as-deposited perovskite films becoming slightly dark, which suggests that air could remove more solvent and promote the intermediate phase transition. By introducing CB vapor into the quenching gas (i.e., air + CB), it is shown that a darker and more uniform as-deposited perovskite film can be observed, indicating that air + CB can realize a better intermediate phase transition and minimize the residual solvent in the as-deposited film.

To further investigate the impacts of the ATS-enhanced gas quenching on the morphology of perovskite films, scanning electron microscopy (SEM) was conducted for the various solvent removal techniques. As shown in Figure 1e, the perovskite films postannealing have an average grain size ≈1 μm. The statistically analyzed grain size is shown in Figure 1f. For the air + CB quenching approach, the average grain size is 1.42 μm, which is larger than that of 1.12 and 0.94 μm for the CB-only and air-only methods, respectively. However, there are some large grains close to 2 μm for the air + CB approach. The increase in grain size may be associated with the faster rate of solvent evaporation and the faster conversion of intermediate phase transitions as discussed above.[28]

The bulk crystallinity of the perovskite films ($Cs_{0.03}FA_{0.97}PbI_{2.96}Br_{0.04}$) was characterized using X-ray diffraction (XRD) as displayed in **Figure 2**a. It is shown that CB, air, and air + CB quench can lead to the cubic, α-phase with a slight PbI_2 peak at $2\theta \approx 12.5°$ due to the excess PbI_2 added in the precursor. To further characterize and investigate the crystalline nature at the surface of the perovskite films, grazing-incidence wide-angle X-ray spectroscopy (GIWAXS) was carried out at an angle of 0.5° for the different quenching conditions (Figure 2d). All films, regardless of the quenching approach, show characteristic Bragg rings at $q = 1.0$ and $q = 2.0$ Å^{-1}, which corresponds to the (110) and (220) diffractions of perovskite, respectively.[29] However, when looking at the derived XRD diffraction patterns for the different quenched films, as shown in Figure 2b,c, there is a clear presence of low-angle peaks ≈5.4°, which are attributed to quasi-2D perovskites.[30–32] This can likely be ascribed to low-dimensional intermediate phases induced and retained from the MACl additivities in the precursor ink.[33] Figure 2c shows the presence of the 2D perovskite peak at 5.38°, where the peak intensity is significantly diminished and then eliminated using the air + CB quench. Although the formation of an intermediate phase is beneficial during crystallization, the retention of this intermediate phase postannealing could form a barrier to charge transfer and reduce the overall device efficiency.[34] As shown in Figure 2e, the CB quench and air quench may lead to a greater portion of intermediate phases present immediately following the quenching. In turn, this leads to an incomplete conversion of the intermediate phases to the photoactive, α-phase, postannealing. On the contrary, following the air + CB quench process can promote conversion of intermediate phases, which leads to the complete conversion of intermediate phase to α-phase following anneal.

To probe the optoelectronic properties of the perovskite layers, we deposited perovskite films on bare glass and collected UV–vis absorption spectra and photoluminescence (PL) measurements of films prepared with different quench techniques as shown in **Figure 3**. The air + CB-quenched perovskite film yields enhanced light absorption ability due to its completed photoactive α-phase transition when compared to the CB or air-quenched films. Additionally, the Tauc plots derived from the UV–vis plots suggest that the air + CB film shifts to a slightly lower bandgap than those of the CB and air-quenched films, potentially due to the elimination of residual 2D intermediate phases. To further investigate the evolution of charge carrier dynamics in the perovskite films, steady-state PL measurements were performed (excited at 643 nm), as shown in **Figure 4**b. The air + CB-quenched film exhibits a stronger PL intensity than those of the CB and air-quenched perovskite films. This increased PL intensity of air + CB-quenched perovskite film indicates that the air + CB quenching resulted in films with fewer defects and reduced nonradiative recombination. Figure 3c shows the t ime-resolved PL (TRPL) spectra of the perovskite films on glass deposited using the different quench methods. Biexponential fitting was used to determine the average carrier recombination lifetime:[35]

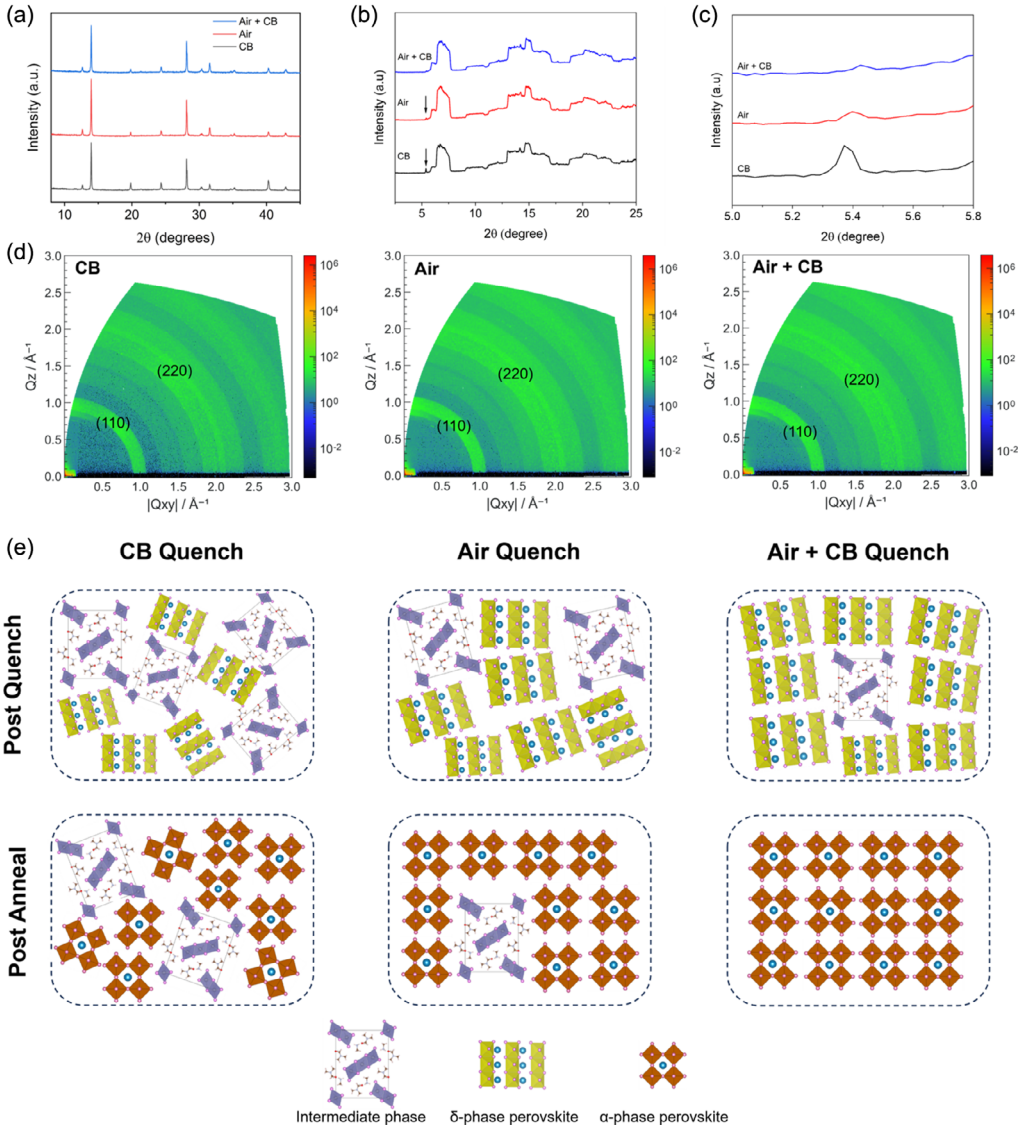

Figure 2. Structure of the ATS-mediated air-quench treated perovskite films. a) XRD patterns of the perovskite films prepared with different quenching methods. b,c) Corresponding to the 2D GIWAXS diffraction patterns collected at 0.5°. d) The 2D GIWAXS patterns of perovskite films based on the CB, air, and air + CB quench methods, e) A graphical explanation illustrating the retained intermediate phase present when using different quench methods.

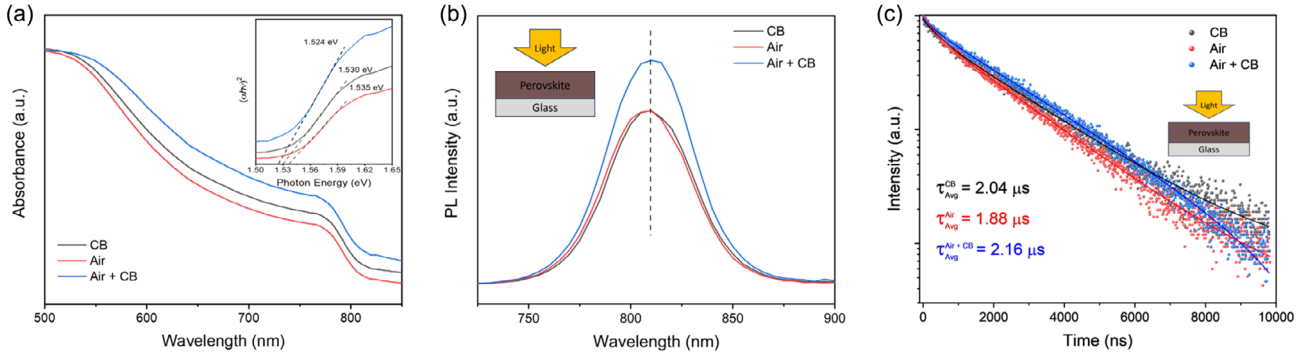

Figure 3. Optoelectronic properties of the ATS-mediated air-quench treated perovskite films. a) UV–vis absorption spectra with inset Tauc plot, b) steady-state PL spectra, and c) TRPL spectra of perovskite films prepared via different quench techniques.

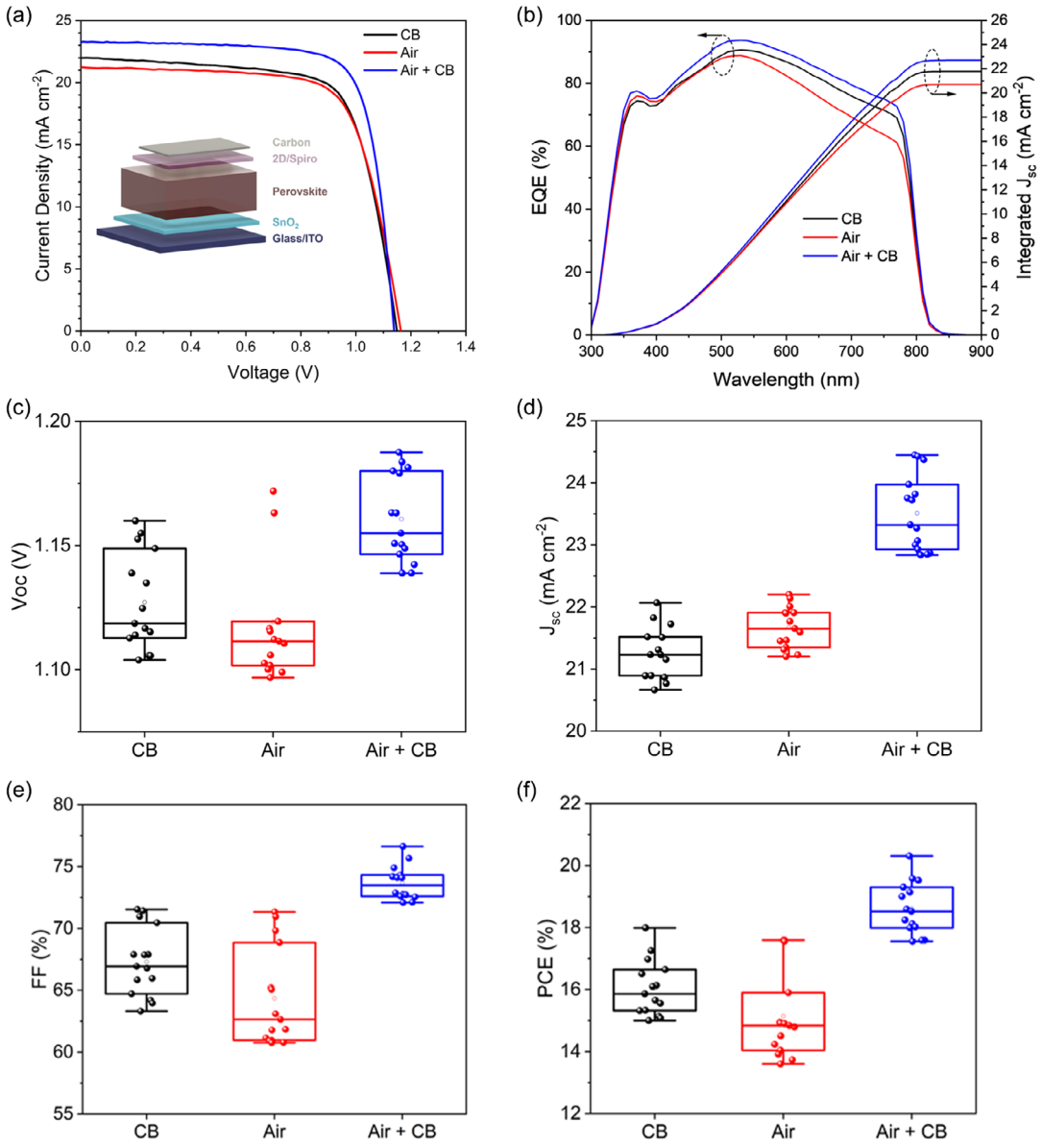

Figure 4. Device performance of the ATS-mediated air-quench treated PSCs. a) *J–V* curves of champion devices prepared under the different quenching conditions (inset of n–*i*–p PSC structure and champion device performance). b) EQE and integrated current density curves for devices prepared under the different quenching conditions. c–f) The statistical distribution diagrams of the photovoltaic parameters of the PSCs prepared using different quenching techniques.

$$f(t) = A_1 \exp\left(-\frac{t}{\tau_1}\right) + A_2 \exp\left(-\frac{t}{\tau_2}\right) + B \quad (1)$$

where τ_1 and τ_2 are the lifetimes for the fast and slow recombination, respectively, A_1 and A_2 are the relative decay amplitude, and B is a constant. The average lifetimes were found to be 2.04, 1.88, and 2.16 µs for the CB, air, and air + CB-quenched specimens, respectively. A table of the parameters derived from the biexponential fitting can be found in Table S2, Supporting Information. The air + CB-quenched film exhibits the longest lifetimes, indicating that the removal of the intermediate phase in the final annealing state is critical for the carrier lifetime time, which may promise a greater chance of the photogenerated carriers being collected during device operation.

Figure 4a shows the current density–voltage (*J–V*) curves of the champion devices (area 0.08 cm^2) prepared using the different quench techniques. The combined air + CB quench technique resulted in a champion PCE of 20.31% with V_{oc} of 1.14 V, J_{sc} of 23.27 mA cm^{-2}, and fill factor (FF) of 76.6%. The device performances of carbon-based planar PSCs fabricated in air using air + CB are also compared to other works and are shown in Figure S2, Supporting Information and supporting information in Table S3, Supporting Information, which shows the historical record efficiencies for C-PSCs.[7,36–62] However,

the CB and air-quench methods for fabricating PSCs in air conditions yielded significantly lower champion PCEs of 18.00% and 17.59% for the CB and air-quenched devices, respectively.

The external quantum efficiency (EQE) measurements for the CB, air, and air + CB-quenched PSCs are shown in Figure 4b. The integrated J_{sc} was found to be 21.78, 20.71, and 22.70 mA cm^{-2} for the CB, air, and air + CB-quenched devices, respectively. While the J_{sc} values derived from the EQE measurements were marginally lower than those obtained from the current-voltage measurements, it is a known phenomenon in PSCs for the J_{sc} from current–voltage measurements to be greater than those obtained from EQE measurements. The difference between the EQE-determined J_{sc} and I–V curve-determined J_{sc} primarily originates from the intrinsic ion migration within the perovskite material itself.[63] Specifically, the air + CB-quenched devices exhibited an improved EQE in the visible light region from 400 to 700 nm compared to the other quenching conditions. This enhancement suggests that the incorporation of CB vapor in the air-quenching gas may promote more photons to be converted to electrons for the visible sunlight by reducing charge recombination and enhancing charge extraction processes.

To evaluate the reliability of this approach, statistical device performance was collected from the best 15 solar cells for each quenching technique (Figure 4c–f). As shown in **Table 1**, the CB-quenched devices exhibited an average V_{oc} of 1.13 V, a J_{sc} of 21.26 mA cm^{-2}, an FF of 67.31%, and a PCE of 16.04%, and the air-quenched devices exhibited an average V_{oc} of 1.10 V, a J_{sc} of 21.20 mA cm^{-2}, an FF of 64.35%, and a PCE of 15.14%. However, the combined air + CB-quenched devices displayed an average V_{oc} of 1.16 V, a J_{sc} of 23.51 mA cm^{-2}, an FF of 74.34%, and a PCE of 18.61%. Hence, the CB-mediated air-quench approach yields significant improvement in all device parameters leading to an overall improvement in PCE. These results underscore the effectiveness of the combinational gas quenching approach in improving the efficiency of C-PSCs prepared in air processing conditions.

To better understand how the combinational air + CB quenching process led to improved device performance, electrical characterization was conducted as shown in **Figure 5**. The dark current–voltage curves are shown in Figure 5a. The dark current density of the air + CB-quenched device is roughly one order of magnitude lower than that of the CB-quenched device and similar to the air-quenched device. This is an indication that the air + CB quenching process can reduce the leakage current due to the photogenerated carriers traveling efficiently through the devices instead of being shunted from electronic transmission channels.[64]

To understand the charge transfer behavior in the air + CB-quenched PSCs, electrochemical impedance spectroscopy (EIS) measurements, as shown in Figure 5b, were collected. The Nyquist plots derived from EIS were obtained by fitting the equivalent circuit shown in the inset. The low-frequency areas of the Nyquist plot correspond to the charge recombination resistance.[65] As shown in the plot, the air + CB-quenched devices show a substantially enhanced charge recombination resistance, indicating that the addition of CB to the air-quenching medium can efficiently inhibit charge recombination in devices prepared in full air processing environments.

Furthermore, capacitance–voltage (C–V) measurements were also collected, and the corresponding Mott–Schottky plots are shown in Figure 5c. The following relationship governs the relationship between the applied potential and the capacitance of the devices.

Table 1. Champion device performance parameters and average device performance parameters in parentheses.

Device	V_{oc} [V]	J_{sc} [mA cm^{-2}]	Fill factor [%]	PCE [%]
CB quench	1.15 (1.13 ± 0.020)	22.04 (21.26 ± 0.43)	70.97 (67.31 ± 2.77)	18.00 (16.04 ± 0.89)
Air quench	1.16 (1.10 ± 0.010)	21.20 (21.67 ± 0.33)	71.34 (64.35 ± 3.97)	17.59 (15.14 ± 1.39)
Air + CB quench	1.14 (1.16 ± 0.017)	23.27 (23.51 ± 0.60)	76.63 (74.34 ± 2.86)	20.31 (18.61 ± 0.84)

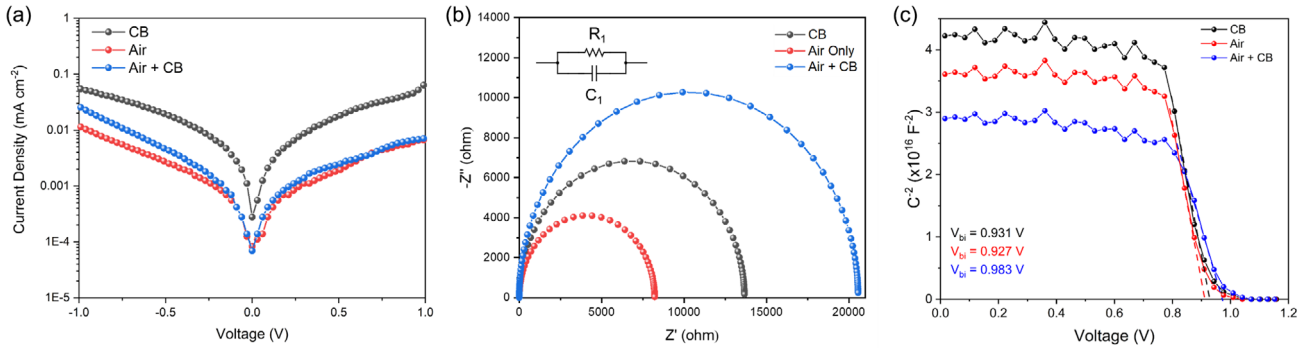

Figure 5. Device physics understanding of the ATS-mediated air-quench treated PSC. a) Dark J–V curves of the PSCs prepared under different quenching conditions, b) EIS derived Nyquist plots of the PSCs with included inset showing the equivalent circuit diagram used for calculation of recombination resistance, and c) Mott–Schottky (MS) measurements for the PSCs.

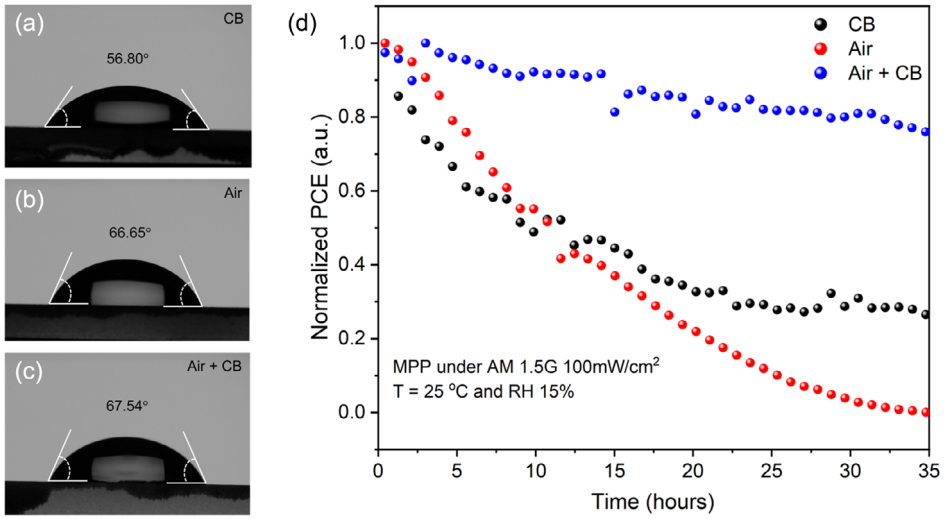

Figure 6. Stability of the ATS-mediated air–gas quench treated PSC. a–c) Contact angle of water on perovskite films treated with CB quench, air quench, and air + CB quench, and d) operation of unencapsulated devices under MPP conditions at 25 °C and 15 RH%.

$$\frac{1}{C^2} = \frac{2}{A^2 q \varepsilon \varepsilon_0 N_D}(V_{bi} - V) \quad (2)$$

where C is the capacitance of the space charge region, ε is the dielectric constant of perovskite, V corresponds to the applied voltage, V_{bi} is the built-in potential, and A is the electrode area.[66] The V_{bi} of the CB, air, and air + CB-quenched devices were found to be 0.931, 0.927, and 0.983 V, respectively, which are in line with the increased V_{oc} in the air + CB-quenched perovskite device. These results also indicate that the combination of air + CB quenching approach leads to significant improvement in charge recombination resistance of the ambient-processed C-PSCs.

To elucidate the role of the air + CB quenching method on the moisture stability of perovskite films, we measured the contact angle of a static water droplet on the surface of perovskite films prepared under different quenching conditions. As shown in **Figure 6**a–c, the contact angle increases for the combined air + CB quenching, which may be ascribed to the enhanced grain size pinhole-free surface of these films, and the reduced PbI_2 residual on the surface as shown in Figure 2b. Thus, the air + CB method may be more effective at minimizing the infiltration of moisture into the perovskite crystal, protecting the film from degradation and maximizing its long-term stability in humid environments. Additionally, we performed maximum power point (MPP) tests at a temperature of 25 °C and relative humidity of 15% for the PSCs prepared under different quenching conditions as shown in Figure 6d. While the CB and air-quenched devices showed a rapid decline in normalized PCE, reaching a t_{S80} in less than 5 h, the air + CB-quenched device was able to retain 80% of its initial efficiency after over 30 h at MPP. The approximately sixfold increase in stability showcases the capabilities of the air + CB quenching approach to improve the robustness of PSCs.

3. Conclusion

In summary, this study presents a newly developed ATS-mediated air-quench technique that enables the efficient fabrication of C-PSCs under ambient conditions. By combining CB vapors with air quenching, we achieved a champion PCE of 20.31% and demonstrated significant improvements in film quality and device stability. The improved efficiency originates from the suppressed intermediate phase residual in the finished perovskite films when using the ATS-mediated air quench. Additionally, the ATS-mediated air-quench approach contributes to an improved carrier lifetime of 2.16 µs and a larger grain size of ≈1.4 µm, reducing the nonradiative recombination in the device and improving the overall performance. Moreover, ambient-processed devices without encapsulation show improved stability during MPP tracking and enhanced hydrophobicity. This approach offers a scalable and cost-effective pathway for the commercial production of C-PSCs, with promising implications for large-scale deployment in photovoltaic applications.

4. Experimental Section

Materials: Lead Iodide (PbI2, 99.99%) was purchased from Tokyo Chemical Industry Company, Ltd. (TCI). Formamidinium iodide (FAI, >98%) and methylammonium chloride (MACl, >98%) were purchased from GreatCell Solar. Tin (IV) oxide (SnO2, 15 wt%) was purchased from BeanTown Chemical. The salts spiro-OMeTAD (99%), Bis(trifluoromethane)sulfonimide lithium salt (LiTFSI, 99.95%), n-hexylammonium bromide (C6Br) and the solvents, N,N-dimethylformamide (DMF, anhydrous 99.8%), dimethyl sulfoxide (DMSO, >99%), chlorobenzene (CB, anhydrous 99.8%), diethyl ether (DEE, 99.5%), toluene (99.8%), and ethanol (>99.5%) were all purchased from Sigma-Aldrich. Isopropyl alcohol (IPA, 99.5%) was purchased from VWR.

PSC Fabrication: Indium-doped SnO_2 (ITO) glass substrates were cleaned with detergent and then cleaned sequentially via ultrasonic baths of deionized water, acetone, and 2-proposal for 15 min, respectively. The ITO substrates were further cleansed through a 20 min UV–Ozone

treatment before the deposition of the 2.67% colloidal SnO_2 electron-transport layer. While inside a fume hood, the SnO_2 dispersion was deposited statically on the surface of the substrate and then spin-coated at 3000 rpm for 30 s. The resulting films were then annealed at 150 °C for 30 min immediately following the deposition. The SnO_2 coated substrates were subsequently treated with UV–Ozone for 20 min before depositing the perovskite absorber layer. The $Cs_{0.03}FA_{0.97}PbI_{2.96}Br_{0.04}$ precursor solution was prepared by mixing PbI_2, FABr, FAI, and CsI in DMF/DMSO (4:1 volume ratio). The perovskite layer was deposited in a fume hood under ambient conditions with moisture less than 50% RH and spin-coated at 1000 rpm for 10 s and then 5000 rpm for 30 s. For the films relying solely on the ATSs, for example, CB was deposited dynamically after 15 s into the high-speed step. For the air-only samples, gas was blown on the surface of the film for 15 s after the first 10 s of the high-speed step using a custom gas nozzle that was fitted to the spin-coater. For the air + CB-quenched samples, the gas was passed through a CB bath in a glass vial and then was blown on the perovskite film during spin coating like the air-only samples. All perovskite films were annealed at 140 °C for 20 min in the fume hood under ambient conditions. After cooling the substrates to room temperature, 60 µL of n-hexylammonium bromide (2.5 mg mL^{-1} in 2-proponal) was deposited dynamically while the substrates spun at 3000 rpm for 30 s. The Spiro-OMeTAD solution was formed by combining Spiro-OMeTAD salt (73.6 mg mL^{-1}) in CB with Li-TFSI (17.5 µL, 520 mg mL^{-1} in acetonitrile) and 4-*t*Bp (28.8 µL). The layer was deposited on the substrate by dropping 30 µL of solution and spinning at 3000 rpm for 30 s. The obtained films were allowed to oxidize overnight in a dry air environment. Finally, a 100 µm thick carbon electrode was applied on top of the Spiro-OMeTAD layer to form top contacts with an area of 0.08 cm^2.

Materials and Device Characterizations: Photo*J–V* were measured using a solar simulator (Newport, Oriel Class AAA 94063A, 1000-Watt Xenon light source) with a Keithley 2420 source meter under simulated AM1.5G (100 mW cm^{-2}, calibrated with a standard Si solar cell) solar irradiation. The active area was defined by a 0.08 cm^2 mask, and the current–voltage scan rate was 100 mV s^{-1}. The EQE was obtained using an EnliTech QE measurement system. The PL and TRPL were acquired using an Edinburgh Instruments FS5 spectrofluorometer. A Paios was used to collect both the *C–V* measurements and the EIS, as well as the dark *J–V* characteristics. The SEM images were obtained using an SEM/focused ion beam from Auriga (Zeiss) at an acceleration voltage of 5 kV. The XRD measurements were recorded by a Rigaku SmartLab high resolution X-ray diffractometer. The GIWAXS measurements were obtained from a Xenocs Xeuss (GI-)SAXS/WAXS/USAXS instrument with a GeniX3D Cu High Flux Very Long (HFVL) focus source as X-ray source and an Eiger2R1M Dectris hybrid pixel silicon sensor as the detector.

Supporting Information

Supporting Information is available from the Wiley Online Library or from the author.

Acknowledgements

This material is based upon work supported by the National Science Foundation (NSF) under grant nos. DMR-2330738, CMMI-2226918, TI-2329871, and ECCS-2413632. Mr. Jacob Wall was sponsored by the NSF Graduate Research Fellowship Program under grant no. 2233001. This material is also based upon work supported by the U.S. Department of Energy's Office of Energy Efficiency and Renewable Energy (EERE) under the Solar Energy Technologies Office award no. DE-EE0009833.

Conflict of Interest

The authors declare no conflict of interest.

Author Contributions

Jacob Wall: Methodology (lead); Validation (lead); Writing—original draft (lead). **Kausar Khawaja**: Data curation (supporting); Methodology (supporting); Writing—review and editing (supporting). **Wenjun Xiang**: Data curation (supporting); Methodology (supporting); Writing—review and editing (supporting). **Adam Dvorak**: Methodology (supporting); Writing—review and editing (supporting). **Christopher Picart**: Methodology (supporting); Writing—review and editing (supporting). **Xiaoyu Gu**: Methodology (supporting); Writing—review and editing (supporting). **Lin Li**: Funding acquisition (supporting); Methodology (supporting); Writing—review and editing (supporting). **Nicholas Rolston**: Funding acquisition (supporting); Methodology (supporting); Supervision (supporting); Writing—review and editing (supporting). **Kai Zhu**: Funding acquisition (supporting); Methodology (supporting); Supervision (supporting). **Joseph J Berry**: Funding acquisition (supporting); Methodology (supporting); Supervision (supporting). **Feng Yan**: Conceptualization (equal); Funding acquisition (lead); Resources (lead); Writing—original draft (supporting); Writing—review and editing (supporting).

Data Availability Statement

The data that support the findings of this study are available from the corresponding author upon reasonable request.

Keywords

air processing, air-quench, antisolvents, carbon electrodes, perovskite solar cells

Received: August 22, 2024
Revised: September 11, 2024
Published online: September 29, 2024

[1] A. Kojima, K. Teshima, Y. Shirai, T. Miyasaka, *J. Am. Chem. Soc.* **2009**, *131*, 6050.
[2] NREL, *Best Research-cell Efficiency Chart*, http://www.nrel.gov/pv/cell-efficiency.html (accessed: July 2024).
[3] M. Younas, T. A. Kandiel, A. Rinaldi, Q. Peng, A. A. Al-Saadi, *Mater. Today Phys.* **2021**, *21*, 100557.
[4] Q. Jiang, J. Tong, R. A. Scheidt, X. Wang, A. E. Louks, Y. Xian, R. Tirawat, A. F. Palmstrom, M. P. Hautzinger, S. P. Harvey, S. Johnston, L. T. Schelhas, B. W. Larson, E. L. Warren, M. C. Beard, J. J. Berry, Y. Yan, K. Zhu, *Science* **2022**, *378*, 1295.
[5] Q. Luo, H. Ma, Q. Hou, Y. Li, J. Ren, X. Dai, Z. Yao, Y. Zhou, L. Xiang, H. Du, H. He, N. Wang, K. Jiang, H. Lin, H. Zhang, Z. Guo, *Adv. Funct. Mater.* **2018**, *28*, 1706777.
[6] D. Zhang, D. Li, Y. Hu, A. Mei, H. Han, *Commun. Mater.* **2022**, *3*, 58.
[7] Y. Wang, W. Li, Y. Yin, M. Wang, W. Cai, Y. Shi, J. Guo, W. Shang, C. Zhang, Q. Dong, H. Ma, J. Liu, W. Tian, S. Jin, J. Bian, Y. Shi, *Adv. Funct. Mater.* **2022**, *32*, 2204831.
[8] Y. Lin, J. Tang, H. Yan, J. Lin, W. Wang, S. Zhang, H. Rao, Z. Pan, X. Zhong, *Energy Environ. Sci.* **2024**, *17*, 4692.
[9] L. Li, Z. Wu, J. Hong, H. Rao, X. Zhong, Z. Pan *ACS Energy Lett.* **2024**, *9*, 4240.
[10] J. Zhang, G. Zhang, P. Su, R. Huang, J. Lin, W. Wang, Z. Pan, H. Rao, X. Zhong, *Angew. Chem. Int. Ed.* **2023**, *62*, e202303486.
[11] L. Li, H. Rao, Z. Wu, J. Hong, J. Zhang, Z. Pan, X. Zhong, *Adv. Funct. Mater.* **2024**, *34*, 2308428.
[12] Y. Cheng, H.-W. Li, J. Qing, Q.-D. Yang, Z. Guan, C. Liu, S. H. Cheung, S. K. So, C.-S. Lee, S.-W. Tsang, *J. Mater. Chem. A* **2016**, *4*, 12748.

[13] B. Conings, A. Babayigit, T. Vangerven, J. D'haen, J. Manca, H.-G. Boyen, *J. Mater. Chem. A* **2015**, *3*, 19123.
[14] M. Li, Y.-M. Xie, X. Xu, Y. Huo, S.-W. Tsang, Q.-D. Yang, Y. Cheng, *Org. Electron.* **2018**, *63*, 159.
[15] X. Wu, D. Zhang, X. Wang, X. Jiang, B. Liu, B. Li, Z. Li, D. Gao, C. Zhang, Y. Wang, Z. Zhu, *EcoMat* **2023**, *5*, e12352.
[16] H. Dong, C. Ran, W. Gao, M. Li, Y. Xia, W. Huang, *eLight* **2023**, *3*, 3.
[17] X. Zhao, W. Gao, H. Dong, Y. Zhou, H. Huang, Z. Wu, C. Ran, *Nano Energy* **2024**, *128*, 109933.
[18] S. T. Williams, F. Zuo, C.-C. Chueh, C.-Y. Liao, P.-W. Liang, A. K.-Y. Jen, *ACS Nano* **2014**, *8*, 10640.
[19] X. Li, M. Ibrahim Dar, C. Yi, J. Luo, M. Tschumi, S. M. Zakeeruddin, M. K. Nazeeruddin, H. Han, M. Grätzel, *Nat. Chem.* **2015**, *7*, 703.
[20] S. D. Stranks, H. J. Snaith, *Nat. Nanotechnol.* **2015**, *10*, 391.
[21] T. A. Berhe, W.-N. Su, C.-H. Chen, C.-J. Pan, J.-H. Cheng, H.-M. Chen, M.-C. Tsai, L.-Y. Chen, A. A. Dubale, B.-J. Hwang, *Energy Environ. Sci.* **2016**, *9*, 323.
[22] A. D. Taylor, Q. Sun, K. P. Goetz, Q. An, T. Schramm, Y. Hofstetter, M. Litterst, F. Paulus, Y. Vaynzof, *Nat. Commun.* **2021**, *12*, 1878.
[23] T. Hou, M. Zhang, W. Yu, X. Wang, Z. Gu, Q. Chen, L. Lan, X. Sun, Y. Huang, B. Zheng, X. Liu, M. A. Green, X. Hao, *J. Mater. Chem. A* **2022**, *10*, 2105.
[24] J. Yin, Y. Lin, C. Zhang, J. Li, N. Zheng, *ACS Appl. Mater. Interfaces* **2018**, *10*, 23103.
[25] V. K. Lamer, R. H. Dinegar, *J. Am. Chem. Soc.* **1950**, *72*, 4847.
[26] B. Ding, Y. Li, S.-Y. Huang, Q.-Q. Chu, C.-X. Li, C.-J. Li, G.-J. Yang, *J. Mater. Chem. A* **2017**, *5*, 6840.
[27] Y. Yun, D. Vidyasagar, M. Lee, O. Y. Gong, J. Jung, H. Jung, D. H. Kim, S. Lee, *Adv. Sci.* **2021**, *8*, 2102492.
[28] S. Liu, V. P. Biju, Y. Qi, W. Chen, Z. Liu, *NPG Asia Mater.* **2023**, *15*, 27.
[29] P. Cheng, P. Wang, Z. Xu, X. Jia, Q. Wei, N. Yuan, J. Ding, R. Li, G. Zhao, Y. Cheng, K. Zhao, S. F. Liu, *ACS Energy Lett.* **2019**, *4*, 1830.
[30] L. Zeng, Z. Chen, S. Qiu, J. Hu, C. Li, X. Liu, G. Liang, C. J. Brabec, Y. Mai, F. Guo, *Nano Energy* **2019**, *66*, 104099.
[31] C. Zuo, A. D. Scully, W. L. Tan, F. Zheng, K. P. Ghiggino, D. Vak, H. Weerasinghe, C. R. Mcneill, D. Angmo, A. S. R. Chesman, M. Gao, *Commun. Mater.* **2020**, *1*, 33.
[32] L. N. Quan, Y. Zhao, F. P. García De Arquer, R. Sabatini, G. Walters, O. Voznyy, R. Comin, Y. Li, J. Z. Fan, H. Tan, J. Pan, M. Yuan, O. M. Bakr, Z. Lu, D. H. Kim, E. H. Sargent, *Nano Lett.* **2017**, *17*, 3701.
[33] J. Chang, E. Feng, H. Li, Y. Ding, C. Long, Y. Gao, Y. Yang, C. Yi, Z. Zheng, J. Yang, *Nano-Micro Lett.* **2023**, *15*, 164.
[34] Z. Wang, Y. Zhou, S. Pang, Z. Xiao, J. Zhang, W. Chai, H. Xu, Z. Liu, N. P. Padture, G. Cui, *Chem. Mater.* **2015**, *27*, 7149.
[35] A. M. Bothwell, C. L. Reich, A. H. Danielson, A. Onno, Z. C. Holman, W. S. Sampath, D. Kuciauskas, *Sol. RRL* **2023**, *7*, 2201029.
[36] N. Ahn, I. Jeon, J. Yoon, E. I. Kauppinen, Y. Matsuo, S. Maruyama, M. Choi, *J. Mater. Chem. A* **2018**, *6*, 1382.
[37] K. Aitola, K. Domanski, J. Correa-Baena, K. Sveinbjörnsson, M. Saliba, A. Abate, M. Grätzel, E. Kauppinen, E. M. J. Johansson, W. Tress, A. Hagfeldt, G. Boschloo, *Adv. Mater.* **2017**, *29*, 1606398.
[38] H. Chen, Z. Wei, H. He, X. Zheng, K. S. Wong, S. Yang, *Adv. Energy Mater.* **2016**, *6*, 1502087.
[39] J. Du, C. Qiu, S. Li, W. Zhang, W. Zhang, Y. Wang, Z. Qiu, Q. Wang, K. Yang, A. Mei, Y. Rong, Y. Hu, H. Han, *Adv. Energy Mater.* **2022**, *12*, 2102229.
[40] J. H. Heo, D. H. Shin, S. Kim, M. H. Jang, M. H. Lee, S. W. Seo, S.-H. Choi, S. H. Im, *Chem. Eng. J.* **2017**, *323*, 153.
[41] I. Jeon, A. Shawky, S. Seo, Y. Qian, A. Anisimov, E. I. Kauppinen, Y. Matsuo, S. Maruyama, *J. Mater. Chem. A* **2020**, *8*, 11141.
[42] Z. Ku, Y. Rong, M. Xu, T. Liu, H. Han, *Sci. Rep.* **2013**, *3*, 3132.
[43] J.-W. Lee, I. Jeon, H.-S. Lin, S. Seo, T.-H. Han, A. Anisimov, E. I. Kauppinen, Y. Matsuo, S. Maruyama, Y. Yang, *Nano Lett.* **2019**, *19*, 2223.
[44] Z. Li, S. A. Kulkarni, P. P. Boix, E. Shi, A. Cao, K. Fu, S. K. Batabyal, J. Zhang, Q. Xiong, L. H. Wong, N. Mathews, S. G. Mhaisalkar, *ACS Nano* **2014**, *8*, 6797.
[45] S. Liu, W. Huang, P. Liao, N. Pootrakulchote, H. Li, J. Lu, J. Li, F. Huang, X. Shai, X. Zhao, Y. Shen, Y.-B. Cheng, M. Wang, *J. Mater. Chem. A* **2017**, *5*, 22952.
[46] Z. Liu, P. You, C. Xie, G. Tang, F. Yan, *Nano Energy* **2016**, *28*, 151.
[47] X. Lu, Y. Li, C. Dong, Y. Gao, G. Yue, K. Liu, Z. Wang, S. Qu, F. Tan, *J. Mater. Res. Technol.* **2023**, *24*, 8162.
[48] A. Mei, X. Li, L. Liu, Z. Ku, T. Liu, Y. Rong, M. Xu, M. Hu, J. Chen, Y. Yang, M. Grätzel, H. Han, *Science* **2014**, *345*, 295.
[49] S. Pandey, A. Kumar, M. Karakoti, K. K. Garg, A. Rana, G. Tatrari, B. S. Bohra, P. Yadav, R. K. Singh, N. G. Sahoo, *Nanoscale Adv.* **2021**, *3*, 4726.
[50] H. Su, J. Xiao, Q. Li, C. Peng, X. Zhang, C. Mao, Q. Yao, Y. Lu, Z. Ku, J. Zhong, W. Li, Y. Peng, F. Huang, Y. Cheng, *Mater. Sci. Semicond. Process.* **2020**, *107*, 104809.
[51] Y. Wang, H. Zhao, Y. Mei, H. Liu, S. Wang, X. Li, *ACS Appl. Mater. Interfaces* **2019**, *11*, 916.
[52] H. Wei, J. Xiao, Y. Yang, S. Lv, J. Shi, X. Xu, J. Dong, Y. Luo, D. Li, Q. Meng, *Carbon* **2015**, *93*, 861.
[53] Z. Wei, H. Chen, K. Yan, X. Zheng, S. Yang, *J. Mater. Chem. A* **2015**, *3*, 24226.
[54] P. You, Z. Liu, Q. Tai, S. Liu, F. Yan, *Adv. Mater.* **2015**, *27*, 3632.
[55] B.-W. Zhang, H.-S. Lin, X.-Y. Qiu, Q.-J. Shui, Y.-J. Zheng, M. Almesfer, E. I. Kauppinen, Y. Matsuo, S. Maruyama, *Carbon* **2023**, *205*, 321.
[56] C. Zhang, S. Wang, H. Zhang, Y. Feng, W. Tian, Y. Yan, J. Bian, Y. Wang, S. Jin, S. M. Zakeeruddin, M. Grätzel, Y. Shi, *Energy Environ. Sci.* **2019**, *12*, 3585.
[57] H. Zhang, Y. Li, S. Tan, Z. Chen, K. Song, S. Huang, J. Shi, Y. Luo, D. Li, Q. Meng, *J. Colloid Interface Sci.* **2022**, *608*, 3151.
[58] H. Zhang, J. Xiao, J. Shi, H. Su, Y. Luo, D. Li, H. Wu, Y. Cheng, Q. Meng, *Adv. Funct. Mater.* **2018**, *28*, 1802985.
[59] J. Zhang, X. Hu, H. Li, K. Ji, B. Li, X. Liu, Y. Xiang, P. Hou, C. Liu, Z. Wu, Y. Shen, S. D. Stranks, S. R. P. Silva, H. Cheng, W. Zhang, *Adv. Funct. Mater.* **2021**, *31*, 2104396.
[60] Q. Zhang, J. Nam, J. Han, S. Datta, N. Wei, E. Ding, A. Hussain, S. Ahmad, V. Skakalova, A. T. Khan, Y. Liao, M. Tavakkoli, B. Peng, K. Mustonen, D. Kim, I. Chung, S. Maruyama, H. Jiang, I. Jeon, E. I. Kauppinen, *Adv. Funct. Mater.* **2022**, *32*, 2103397.
[61] X. Zheng, H. Chen, Z. Wei, Y. Yang, H. Lin, S. Yang, *Front. Optoelectron.* **2016**, *9*, 71.
[62] H. Zhou, Y. Shi, Q. Dong, H. Zhang, Y. Xing, K. Wang, Y. Du, T. Ma, *J. Phys. Chem. Lett.* **2014**, *5*, 3241.
[63] M. Saliba, L. Etgar, *ACS Energy Lett.* **2020**, *5*, 2886.
[64] J. Duan, Y. Wang, X. Yang, Q. Tang, *Angew. Chem. Int. Ed.* **2020**, *59*, 4391.
[65] J. Yang, H. Yu, S. Wu, C. Cai, J. Gao, X. Lu, X. Gao, L. Shui, S. Wu, J.-M. Liu, *ACS Appl. Energy Mater.* **2022**, *5*, 2881.
[66] D. Zheng, F. Yi, Q. Zhang, Q. Guo, Q. Tang, J. Duan, *Energy Technol.* **2022**, *10*, 2200290.